

## Raman intensity of single-wall carbon nanotubes

R. Saito, T. Takeya, and T. Kimura

*Department of Electronics Engineering, University of Electro-Communications, Chofugaoka, Chofu, 182-8585 Tokyo, Japan*

G. Dresselhaus and M. S. Dresselhaus

*Department of Physics, Massachusetts Institute of Technology, Cambridge, Massachusetts 02139*

(Received 26 August 1997)

Using nonresonant bond-polarization theory, the Raman intensity of a single-wall carbon nanotube is calculated as a function of the polarization of light and the chirality of the carbon nanotube. The force-constant tensor for calculating phonon dispersion relations in the nanotubes is scaled from those for two-dimensional graphite. The calculated Raman spectra do not depend much on the chirality, while their frequencies clearly depend on the nanotube diameter. The polarization and sample orientation dependence of the Raman intensity shows that the symmetry of the Raman modes can be obtained by varying the direction of the nanotube axis, keeping the polarization vectors of the light fixed.

[S0163-1829(98)06908-2]

### I. INTRODUCTION

An important advance in carbon nanotube science<sup>1</sup> is the synthesis of single-wall carbon nanotubes (SWCN's) in high yield using the laser ablation method with transition-metal catalysts, in which a bundle of SWCN's forms a triangular lattice of nanotubes, known as a *rope*.<sup>2,3</sup> Using such nanotube ropes, several solid state properties pertaining to a single nanotube have been observed. In particular, Rao *et al.*<sup>4</sup> have reported Raman spectra for SWCN's in which they assigned the observed Raman modes with specific  $(n,m)$  nanotubes known to be present in their samples. They showed that the Raman signal from the rope not only consists of the graphite-oriented  $E_{2g}$  (or  $E_g$ ) modes, which occur around  $1550\text{--}1600\text{ cm}^{-1}$ , but also contains a strong low-frequency  $A_g$ -active mode, known as the nanotube radial breathing mode, which is special to the nanotube geometry. Within the bond-polarization theory, they have assigned this spectral contribution as coming from armchair nanotubes,<sup>5,6</sup> which are denoted by the chiral vectors<sup>4-6</sup>  $(n,n)$  for  $n=8,9$ , and 10. The authors, however, did not consider the case of other chiral nanotubes in their theoretical analysis.

Recently Kataura *et al.*<sup>7</sup> reported that various chiral nanotubes with almost all possible nanotube chiral angles are expected from the assignment of the observed Raman spectra to the calculated  $A_{1g}$  breathing modes,<sup>8</sup> under different synthesis conditions through variation of the catalyst composition and the furnace temperature. According to their results,<sup>7</sup> smaller diameter nanotubes are obtained by lowering the furnace temperature to the range of  $1000\text{--}1200\text{ }^\circ\text{C}$  and using a Rh/Pd catalyst instead of the Ni/Co catalyst that was used to prepare the samples in Ref. 4.

As for the distribution in chiral angle of carbon nanotubes prepared by the method in Refs. 3 and 4, Cowley *et al.* showed from TEM experiments that the observed range of chiral angle lies within  $7.3^\circ$  from the armchair angle.<sup>9</sup> Thus it is interesting to examine the Raman spectra for chiral nanotubes theoretically.

The group theory for carbon nanotubes predicts that there

are 15 or 16 Raman-active modes at  $k=0$  for all armchair  $(n,n)$ , zigzag  $(n,0)$ , and chiral  $(n,m)$  ( $n \neq m$ ) nanotubes.<sup>1,8</sup> The number of Raman-active modes does not depend on the number of carbon atoms in the unit cell, which is given by  $2N=4(n^2+m^2+nm)/d_R$  for  $(n,m)$  nanotubes.<sup>1</sup> Here  $d_R$  is the highest common divisor of  $(2m+n)$  and  $(2n+m)$ . A simple explanation for why we get almost the same number of Raman modes for any nanotube is as follows: For lower Raman frequencies, the vibrations can "see" only the cylindrical surface, while for higher Raman frequencies, the vibrations see only the local  $sp^2$ -bond structure of graphite, which is the same for any nanotube. However, the chirality of the nanotube may affect the Raman frequency, as we will show below.

Another interesting point concerns polarization effects in the Raman spectra, which are commonly observed in low-dimensional materials. Since nanotubes are one-dimensional materials, the use of light polarized parallel or perpendicular to the tube axis will give information about the low dimensionality of the nanotubes. The availability of purified samples of aligned nanotubes would allow us to obtain the symmetry of a mode directly from the measured Raman intensity by changing the experimental geometry, such as the polarization of the light and the sample orientation, as discussed in this paper.

The enhancement of the Raman intensity is observed as a function of laser frequency when the excitation frequency is close to a frequency of high "optical" absorption and this effect is called the resonant Raman effect. The observed Raman spectra of SWNT's show resonant Raman effects,<sup>4</sup> which reflect the one-dimensional van Hove singularities of the electronic density of states (DOS) of the  $\pi$  bands. The resonant Raman effect is expected to be observed clearly in carbon nanotubes when the singularities in the one-dimensional density of electronic states are separated from each other in the DOS spectra. The number of singularities in the DOS spectra of a nanotube depends on the number of  $\pi$  energy subbands  $2N$ , where  $N$  is the number of carbon atoms in the unit cell defined above. Thus nanotubes with small  $N$ ,

such as the achiral nanotubes and chiral nanotubes with large  $d_R$ , may show a clear resonance effect when the frequency of the laser light is tuned. On the other hand, chiral nanotubes with large  $N$  may not show the resonance effect. Since the number  $N$  depends strongly on the chirality, the resonant Raman intensity depends on the chirality. The different resonant energies come from the electronic structure of the constituent nanotubes of the sample, which have different diameters and chiralities. Since the Raman modes can be reasonably well identified for a single chirality nanotube, such a resonant effect from a mixed sample emphasizes effects associated with a distribution of nanotube radii. Though the present theory is within a nonresonant scheme so that it cannot be used to obtain the resonant spectra explicitly, we believe that our model nevertheless gives important information about the Raman modes for nanotubes with different diameters and chiralities.

In Sec. II we first show the method for calculating the phonon dispersion relations in carbon nanotubes and in Sec. III the calculated Raman intensities for different chiral nanotubes are presented as a function of the polarization of the light and the relative orientation of the nanotube axis with respect to the polarization vector. Finally, a summary of the findings is given in Sec. IV.

## II. METHOD

### A. Force-constant model

A general approach for obtaining the phonon dispersion relations of carbon nanotubes is given by the zone-folding method, whereby the phonon dispersion relations of a two-dimensional (2D) graphene sheet are folded into the one-dimensional Brillouin zone<sup>10</sup> for the carbon nanotube. However, in the zone-folding method, special corrections are necessary, especially for the lower-frequency phonon modes, since some phonon modes of SWCN's cannot be expressed by the zone-folded phonon modes of 2D graphite.<sup>10</sup> This comes from the fact that the in-plane and out-of-plane modes are decoupled in the 2D graphite phonon modes, but that is not the case for a nanotube. In order to avoid this difficulty, tight-binding molecular dynamics are adopted for the nanotube geometry, in which the atomic force potential for general carbon materials is used.<sup>4,8</sup> Here we use the scaled force constants from those of 2D graphite and we construct a force-constant tensor for a constituent atom of the SWCN so as to satisfy the rotational sum rule for force constants.<sup>11</sup>

In general, the equations of motion for the displacement of the  $i$ th coordinate,  $\vec{u}_i = (x_i, y_i, z_i)$  for  $N$  atoms in the unit cell, are given by

$$M_i \ddot{\vec{u}}_i = \sum_j K^{(ij)} (\vec{u}_j - \vec{u}_i) \quad (i = 1, \dots, N), \quad (1)$$

where  $M_i$  is the mass of the  $i$ th atom and  $K^{(ij)}$  represents the  $3 \times 3$  force-constant tensor that couples the  $i$ th and  $j$ th atoms. The sum over  $j$  in Eq. (1) is normally taken over only a few neighbor distances relative to the  $i$ th site, which for a 2D graphene sheet has been carried out up to fourth-nearest-neighbor interactions.<sup>10</sup> Using the Fourier transform of the displacements  $\vec{u}_i$ , we get a  $3N \times 3N$  dynamical matrix  $\mathcal{D}(\vec{k})$ , which satisfies

$$\mathcal{D}(\vec{k}) \vec{u}_{\vec{k}} = 0. \quad (2)$$

To obtain the eigenvalues  $\omega^2(\vec{k})$  for  $\mathcal{D}(\vec{k})$  and the nontrivial eigenvectors  $\vec{u}_{\vec{k}} \neq \vec{0}$ , we solve the secular equation  $\det \mathcal{D}(\vec{k}) = 0$  for a given  $\vec{k}$  vector. It is convenient to divide the full dynamical matrix  $\mathcal{D}(\vec{k})$  into small  $3 \times 3$  matrices  $\mathcal{D}^{(ij)}(\vec{k})$  ( $i, j = 1, \dots, N$ ), where we denote the dynamical matrix  $\mathcal{D}(\vec{k})$  by  $\{\mathcal{D}^{(ij)}(\vec{k})\}$  and it follows that  $\mathcal{D}^{(ij)}(\vec{k})$  is expressed as

$$\mathcal{D}^{(ij)}(\vec{k}) = \left( \sum_{j''} K^{(ij'')} - M_i \omega^2(\vec{k}) I \right) \delta_{ij} - \sum_{j'} K^{(ij')} e^{i\vec{k} \cdot \Delta \vec{R}_{ij'}}, \quad (3)$$

where the sum over  $j''$  is taken for all neighbor sites (relative to the  $i$ th atom) with  $K^{(ij'')} \neq 0$  and the sum over  $j'$  is only taken over the sites equivalent to the  $j$ th atom.

Since we have  $2N$  carbon atoms, the dynamical matrix to be solved becomes a  $6N \times 6N$  matrix. In analogy to graphite, the hexagonal lattice of a nanotube consists of two sublattices denoted by  $A$  and  $B$ . Here we denote the  $2N$  atoms as  $A_i$  and  $B_j$  ( $i, j = 1, \dots, N$ ), where the  $NA_i$  (or  $NB_j$ ) atoms are geometrically equivalent to one another. This equivalence reduces the calculation of the force-constant tensor as follows. When we divide the full  $6N \times 6N$  dynamical matrix into the  $3 \times 3$  small matrices  $\mathcal{D}^{(A_i B_j)}$  for a pair of  $A_i$  and  $B_j$  atoms, we then consider  $(2N)^2 = 4N^2$  small matrices  $\mathcal{D}^{(A_i A_j)}$ ,  $\mathcal{D}^{(A_i B_j)}$ ,  $\mathcal{D}^{(B_i A_j)}$ , and  $\mathcal{D}^{(B_i B_j)}$  ( $i, j = 1, \dots, N$ ), in which interactions only up to fourth-nearest-neighbor pairs are considered. The corresponding force-constant tensor  $K^{(A_p B_q)}$  can be generated using

$$K^{(A_p B_q)} = (U^{-1})^{p-1} K^{(A_1 B_{q-p+1})} U^{p-1}, \quad (4)$$

where  $U$  is a unitary matrix for rotation by an angle  $\Psi = 2\pi/N$  around the nanotube axis and  $U^{p-1}$  is defined as

$$U^{p-1} = \begin{pmatrix} \cos(p-1)\Psi & \sin(p-1)\Psi & 0 \\ -\sin(p-1)\Psi & \cos(p-1)\Psi & 0 \\ 0 & 0 & 1 \end{pmatrix}, \quad (5)$$

where the  $z$  axis is taken for the nanotube axis. When  $(q-p+1)$  is negative or zero in Eq. (4) we use  $(N+q-p+1)$  for  $(q-p+1)$ . When the value of  $p$  goes from 1 to  $N$ , we go over all  $A_p$  atoms once in the unit cell. Thus we can generate all force-constant tensors from the nonzero tensors related to  $A_1$  or  $B_1$ , such as  $K^{(A_1 A_p)}$ ,  $K^{(A_1 B_p)}$ ,  $K^{(B_1 A_p)}$ , and  $K^{(B_1 B_p)}$ .

The force-constant tensor  $K^{(A_1 B_p)}$  is generated by rotating the chemical bond  $A_1 B_p$  from the two-dimensional plane to the three-dimensional coordinates of the nanotube, as shown in Fig. 1. We now explain how to rotate the bond  $A_1 B_1$ . At first the atom  $A_1$  is on the  $x$  axis and  $B_1$  is at an open circle in the  $xy$  plane, as shown in Fig. 1(a). We move the  $B_1$  atom from the  $xy$  plane to another open circle as shown in Fig. 1(a) by rotating by  $\pi/6 - \theta$  around the  $x$  axis, where  $\theta$  is the chiral angle defined by  $\theta = \tan^{-1}[\sqrt{3}m/(m+2n)]$ . Then in the top view of Fig. 1(b), we rotate  $B_1$  from the open circle to the solid circle by an angle  $\varphi/2$  around  $A_1$ , where  $\varphi$  is

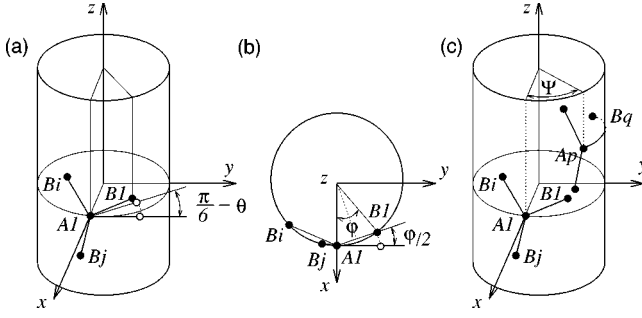


FIG. 1. Rotations of the chemical bonds from the two-dimensional plane to the cylindrical surface. The force constant matrix is generated by performing the corresponding set of rotations on a second-rank tensor. See details in the text.

defined by the angle between A1 and B1 around the  $z$  axis. This notation allows us to put the B1 atom on the cylindrical surface of the nanotube. Finally, we rotate A1 and B1 around the  $z$  axis by the angle  $\Psi$  in Eq. (5) as discussed above [Fig. 1(c)]. The force constant matrix in the new coordinate system is generated by the corresponding rotation of the second rank tensor in which the two-dimensional graphite force-constant parameters<sup>10</sup> are used.

Multiplying the force-constant tensor thus obtained by  $\exp(ik\Delta z_{ij})$ , where  $\Delta z_{ij}$  is the component of  $\Delta \vec{R}_{ij}$  along the  $z$  or nanotube axis, the dynamical matrix is obtained as a function of the wave vector  $k$  [see Eq. (3)]. The phonon energy dispersion relation  $\omega(k)$  is obtained by solving the dynamical matrix of Eq. (3) for many  $k$  points in the one-dimensional Brillouin zone.

It should be mentioned that the effect of curvature is not perfectly included in the force constants thus obtained and the calculated frequency at  $k=0$  for the rotational acoustic mode is not zero as it must be, but rather has a finite value [ $\sim 4 \text{ cm}^{-1}$  for the (10,10) nanotube]. It is clear that the rotational motions of the two neighboring atoms are not parallel to the chemical bonds between the two atoms and this effect gives an artificial out-of-plane force using the method described above. To avoid this unphysical result, we scaled the force-constant parameters<sup>10</sup> by the formulas:

$$\begin{aligned}\phi'_{t'o} &= \phi_{t'o} + \phi_{t'o} \left[ 1 - \cos\left(\frac{\varphi}{2}\right) \right], \\ \phi'_r &= \phi_r + \phi_r \cos\left(\frac{\pi}{6} - \theta\right) \left[ 1 - \cos\left(\frac{\varphi}{2}\right) \right], \\ \phi'_{ti} &= \phi_{ti} + \phi_{ti} \sin\left(\frac{\pi}{6} - \theta\right) \left[ 1 - \cos\left(\frac{\varphi}{2}\right) \right],\end{aligned}\quad (6)$$

where the  $\phi'_{t'o}$  and  $\phi_{t'o}$  are, respectively, the scaled and the original force-constant parameters, and a similar notation is used for the force constant parameters  $\phi_r$  and  $\phi_{ti}$ . The idea for using this scaled force-constant approach comes from the fact that we recover a reduction in the force due to the different directions of the force defined for the chemical bond in free space from the force on the cylindrical surface. When we make these corrections to the force constant using Eq. (6), we always get the correct vanishing of the purely rotational mode frequencies at  $k=0$  for any nanotube, and this condition is necessary in order to satisfy the rotational sum rule for the force constants.<sup>11</sup> As for the other phonon frequencies, the frequencies at the  $\Gamma$  point shift by at most  $4 \text{ cm}^{-1}$  in the lowest  $E_{2g}$  mode resulting from the correction to the force-constant parameters for a (10,10) nanotube associated with Eq. (6). As for the higher-frequency modes, the correction to these frequencies is very small. We emphasize that although the magnitude of the corrections in Eq. (6) is small, this correction is important to ensure that the symmetry conditions for translations of the centers of mass and rotations about the center of mass are correctly satisfied.

## B. Raman intensity

Using the calculated phonon modes of a SWCN, the Raman intensities of the modes are calculated within the non-resonant bond-polarization theory, in which empirical bond polarization parameters are used.<sup>12</sup> The bond parameters that we used in this paper are listed in Table I. In the table we also list the Raman polarizability parameters that are used for carbon atoms. In order to obtain these parameters, we start from the values for the bond polarizability that were used for

TABLE I. Raman polarizability parameters for various carbon-related molecules. The bond lengths of C—C and C=C for  $C_{60}$  and C=C for SWNT are 1.46, 1.40, and 1.44 Å, respectively, and  $\alpha'$  denotes the derivative of  $\alpha$ .

Molecule	Bond	$\alpha_{\parallel} + 2\alpha_{\perp}$ (Å <sup>3</sup> )	$\alpha_{\parallel} - \alpha_{\perp}$ (Å <sup>3</sup> )	$\alpha'_{\parallel} + 2\alpha'_{\perp}$ (Å <sup>2</sup> )	$\alpha'_{\parallel} - \alpha'_{\perp}$ (Å <sup>2</sup> )
CH <sub>4</sub> <sup>a</sup>	C—H	1.944			
C <sub>2</sub> H <sub>6</sub> <sup>a</sup>	C—C	2.016	1.28	3.13	2.31
C <sub>2</sub> H <sub>4</sub> <sup>a</sup>	C=C	4.890	1.65	6.50	2.60
C <sub>60</sub> <sup>b</sup>	C—C		1.28	2.30 ± 0.01	2.30 ± 0.30
	C=C		0.32 ± 0.09	7.55 ± 0.40	2.60 ± 0.36
C <sub>60</sub> <sup>a</sup>	C—C		1.28 ± 0.20	1.28 ± 0.30	1.35 ± 0.20
	C=C		0.00 ± 0.20	5.40 ± 0.70	4.50 ± 0.50
SWNT <sup>c</sup>	C=C		0.04	4.7	4.0

<sup>a</sup>Reference 12.

<sup>b</sup>Reference 13.

<sup>c</sup>Present work.

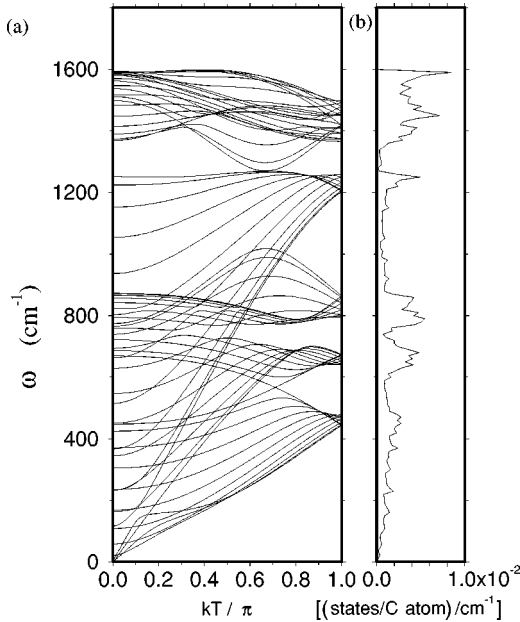


FIG. 2. (a) Calculated phonon dispersion relations of an armchair carbon nanotube with  $\bar{C}_h = (10,10)$ . The number of degrees of freedom is 120 and the number of distinct phonon branches is 66. (b) Phonon density of states of (10,10) nanotubes.

$C_{60}$  (Refs. 12 and 13) and other materials for single (1.46 Å) and double (1.40 Å) carbon bonds and we interpolate between these values to obtain an estimate for the bond-polarizability parameters for SWCN's. We then adjust these parameters so as to reproduce the Raman signal for randomly oriented nanotubes. Although the values thus obtained are within a reasonable range, the values listed in Table I for the various carbon materials show considerable scatter.

It is known, however, that the polarizability parameters of carbon are similar for a variety of carbon materials. Furthermore, the relative intensities for the Raman modes are not so sensitive to small changes in the values of the bond-polarization parameters except for the lowest  $E_{2g}$  mode. Only the lowest  $E_{2g}$  mode is found to be sensitive to the bond-polarization parameter  $\alpha_{\parallel} - \alpha_{\perp}$ . Thus the fitted values listed in Table I were used for the present calculation. The Raman intensity is calculated using the eigenvectors for the vibrational modes, obtained by solving the dynamical matrix, and the polarizability parameters are obtained using bond-polarization theory.<sup>12</sup>

### III. CALCULATED RESULTS

#### A. Phonon dispersion relations

The results thus obtained for  $\omega(k)$  for a (10,10) armchair carbon nanotube are given in Fig. 2(a), where  $T$  denotes the unit vector along the tube axis.<sup>1</sup> For the  $2N=40$  carbon atoms per circumferential strip for the (10,10) nanotube, we have 120 vibrational degrees of freedom, but because of mode degeneracies there are only 66 distinct phonon branches, for which 12 modes are nondegenerate and 54 are doubly degenerate. We also show the phonon density of states for (10,10) in Fig. 2(b). Here we integrated the states with an accuracy of  $10 \text{ cm}^{-1}$ . The phonon density of states

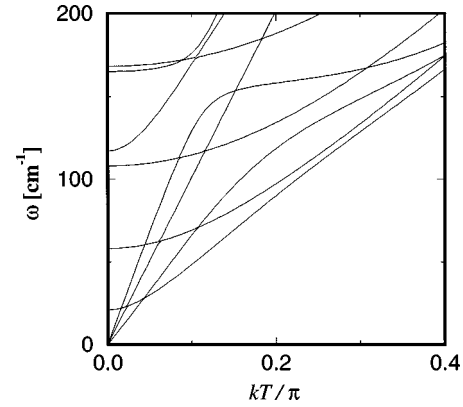


FIG. 3. Phonon dispersion relations shown on an expanded scale for a (10,10) carbon nanotube near the  $\Gamma$  point ( $k=0$ ).

is close to that for 2D graphite except for the small peaks due to the one-dimensional singularities.

Let us focus our attention on the acoustic modes of the (10,10) carbon nanotube. In Fig. 3 the phonon dispersion relations around the  $\Gamma$  point are shown on an expanded scale for the (10,10) carbon nanotube. The lowest-energy modes near  $k=0$  are the transverse-acoustic (TA) modes, which are doubly degenerate, and have  $x$  and  $y$  displacements perpendicular to the nanotube ( $z$ ) axis. The highest-energy mode is the longitudinal-acoustic (LA) mode whose displacement exists in the direction of the nanotube axis. Since the displacements of the three acoustic modes are three dimensional, the frequencies of the phonon dispersion relations are proportional to  $k$  for all three phonon branches, as is commonly observed in the solid state. The sound velocities of the TA and LA phonons for a (10,10) carbon nanotube,  $v_{TA}^{(10,10)}$  and  $v_{LA}^{(10,10)}$ , are estimated as  $v_{TA}^{(10,10)} = 9.42 \text{ km/s}$  and  $v_{LA}^{(10,10)} = 20.35 \text{ km/s}$ , respectively. Since the TA mode of every nanotube has both an “in-cylindrical-plane” and an “out-of-cylindrical-plane” component, the TA modes of the nanotube are softer than the TA or LA modes of 2D graphite. On the other hand, the LA mode of the nanotube has only an in-plane component mode that is comparable in slope to the LA mode of 2D graphite. In fact, with the force-constant parameters that are used in this paper, we have calculated the phonon dispersion relations of 2D graphite, which give  $v_{TA}^G = 15.00 \text{ km/s}$  and  $v_{LA}^G = 21.11 \text{ km/s}$  for the in-plane TA and LA modes, respectively. The calculated phase velocity of the out-of-plane TA mode for 2D graphite is almost 0 km/s because of its  $k^2$  dependence. It is clear that the  $v_{TA}^{(10,10)}$  that has an out-of-plane component is smaller than the purely in-plane  $v_{TA}^G$ . Further, the sound velocities of 2D graphite do not depend on the direction in the graphitic plane because of the threefold symmetry in the hexagonal lattice. However, since the threefold symmetry is broken in carbon nanotubes, we expect a chirality dependence of the sound velocity on  $v_{LA}^{SWCNT}$  and so on. This effect will be reported elsewhere.

From the value for  $v_{LA}^{(10,10)}$ , the elastic constant,  $C_{11}$ , where 1 denotes  $zz$ , can be estimated by  $v_{LA} = \sqrt{C_{11}/\rho}$ , in which  $\rho$  is the mass density of the carbon atoms. When we assume a triangular lattice of nanotubes with lattice constants<sup>3</sup>  $a = 16.95 \text{ Å}$  and  $c = 1.44 \times \sqrt{3} \text{ Å}$ , the mass density  $\rho$  becomes  $1.28 \times 10^3 \text{ kg/m}^3$ , from which we obtain

Young's modulus  $C_{11}=530$  GPa. Young's modulus is almost the same as  $C_{11}$  since  $C_{12}$  is expected to be much smaller than in 2D graphite.<sup>14</sup> This value is much smaller than  $C_{11}=1060$  GPa (Ref. 15) and the range discussed by several other groups,<sup>16,17</sup> and the difference in the estimate for Young's modulus is due to the smaller values for the mass density.

In addition, there is a fourth acoustic mode for the carbon nanotube, which is related to a rotation around the nanotube axis at  $k=0$ . Since the force driving this wave motion is a twisting motion of the nanotube,<sup>4</sup> we call this mode a twisting mode. The velocity of the twisting acoustic wave is estimated to be 15.00 km/s for a (10,10) nanotube. This value is equal to the calculated velocity of  $v_{TA}^G$  for a graphene sheet since the twisting mode is an in-cylindrical-plane mode. It is noted that the sound velocities that we have calculated for 2D graphite are similar to those observed in 3D graphite,<sup>15</sup> for which  $v_{TA}^{G3D}=12.3$  km/s and  $v_{LA}^{G3D}=21.0$  km/s. Although there is some difference in the sound velocities calculated by various groups, the present calculation gives good results for the Raman mode frequencies as shown below.

It is interesting to note that the lowest phonon mode with nonzero frequency at  $k=0$  is not a nodeless  $A_{1g}$  mode, but rather an  $E_{2g}$  mode with two nodes in which the cross section of the carbon nanotube is vibrating with the symmetry described by the basis functions of  $x^2-y^2$  and  $xy$ . The calculated frequency of the  $E_{2g}$  mode for the (10,10) carbon nanotube is  $17\text{ cm}^{-1}$ . Although this mode is a Raman-active mode, there is at present no experimental observation of this mode. Possible reasons why this mode has not yet been observed is that the frequency may be too small to be observed because of the strong Rayleigh scattering or that the frequency of the  $E_{2g}$  mode may be modified by the effect of internanotube interactions.

The strongest low-frequency Raman mode is the radial breathing  $A_{1g}$  mode whose frequency is calculated to be  $165\text{ cm}^{-1}$  for the (10,10) nanotube. Since this frequency is in the silent region for graphite and other carbon materials, this  $A_{1g}$  mode provides a good marker for specifying the carbon nanotube geometry. Another merit of the  $A_{1g}$  mode is that the  $A_{1g}$  frequency is sensitive to the nanotube diameter  $d_t$  or radius  $r$ . In Fig. 4 we give the calculated lower Raman-active mode frequencies as a function of the carbon nanotube radius  $r$  on a log-log plot for  $(n,m)$  in the range  $8 \leq n \leq 10$ ,  $0 \leq m \leq n$ . Figure 4 clearly shows straight-line dependences on  $r$  for all four Raman modes, showing a power dependence of  $\omega(r)$  on  $r$ , but no chirality dependence, which is consistent with the fact that the energy gap of a semiconducting nanotube and the strain energy depend only on the nanotube radius.<sup>18,19</sup> From the slopes of  $\omega(r)$  for this range of  $r$ , we conclude that, except for the lowest  $E_{2g}$  mode, the frequencies are inversely proportional to  $r$  within only a small deviation. This dependence is closely related to the circumferential length of the nanotube. As for the lowest  $E_{2g}$  mode, the frequency  $\omega_{2g}(r)$  has a dependence of  $r^{-1.95 \pm 0.03}$ , which is approximately quadratic, and may reflect the curvature effect of the nanotube. The fitted power law for the  $A_{1g}$  mode that is valid in the region  $3 \text{ \AA} \leq r \leq 7 \text{ \AA}$ :

$$\omega(r) = \omega_{(10,10)} \left( \frac{r_{(10,10)}}{r} \right)^{1.0017 \pm 0.0007}, \quad (7)$$

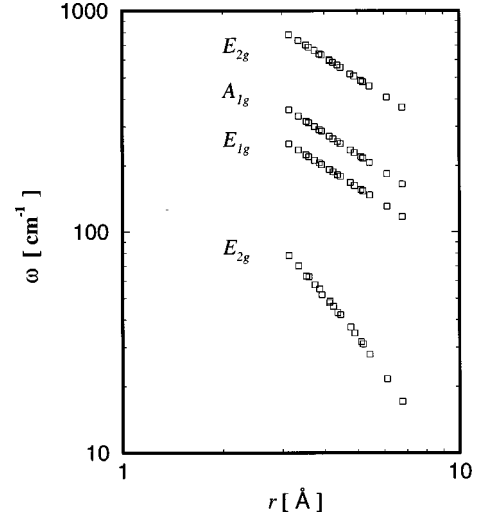


FIG. 4. A log-log plot of the lower Raman mode frequencies as a function of carbon nanotube radius.

should be useful to experimentalists. Here  $\omega_{(10,10)}$  and  $r_{(10,10)}$  are, respectively, the frequency and radius of the (10,10) armchair nanotube, with values of  $\omega_{(10,10)}=165\text{ cm}^{-1}$  and  $r_{(10,10)}=6.785\text{ \AA}$ , respectively.

It is noted that the  $E_{1g}$  and  $A_{1g}$  modes exist in a similar frequency region. However, since the intensity of the  $E_{1g}$  modes is not as strong as that for the  $A_{1g}$  mode, the experimental Raman spectra between 100 and  $300\text{ cm}^{-1}$  are dominated by the  $A_{1g}$  mode. As for the higher-frequency Raman modes, we do not see a strong dependence on  $r$  since the frequencies of the higher optical modes are more sensitively determined by the local movements of the atoms.

## B. Raman intensity of nanotubes

The Raman intensity for the various Raman-active modes in carbon nanotubes is calculated at a phonon temperature of 300 K, which appears in the formula for the Bose distribution function for phonons. The eigenfunctions for the various vibrational modes are calculated numerically at the  $\Gamma$  point ( $k=0$ ).

### 1. The chirality dependence of the Raman intensity as a function of the polarization of the light

In Fig. 5 we show the calculated Raman intensities for the (10,10) armchair, (17,0) zigzag, and (11,8) chiral nanotubes, whose radii are, respectively,  $6.78\text{ \AA}$ ,  $6.66\text{ \AA}$ , and  $6.47\text{ \AA}$  and are close to one another. Here the Raman intensity is averaged over the sample orientation of the nanotube axis relative to the Poynting vector, in which the average is calculated by summing over the many possible directions, weighted by the solid angle for that direction. Here we consider two possible geometries for the polarization of the light: the  $VV$  and  $VH$  configurations. In the  $VV$  configuration, the incident and the scattered polarizations are parallel to each other, while they are perpendicular to each other in the  $VH$  direction. Generally the cross section for Raman scattering is a function of the scattered angle of the light. However the formula of the bond polarization theory consid-

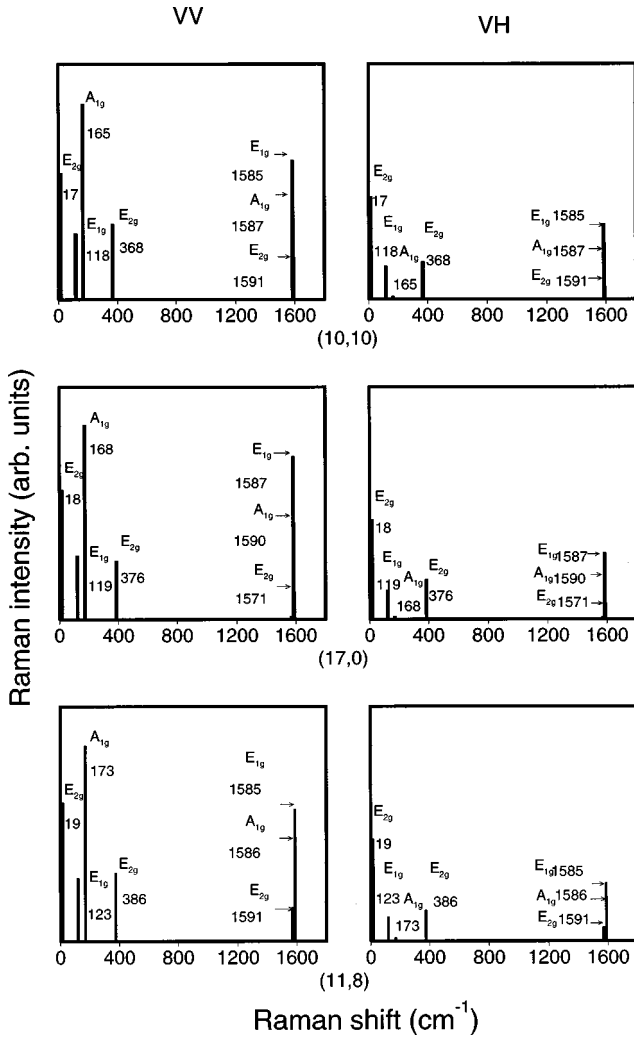


FIG. 5. Polarization dependence of the Raman scattering intensity for (10,10) armchair (top), (17,0) zigzag (middle), and (11,8) chiral (bottom) nanotubes. The left column is for the  $VV$  scattering configuration and the right column is for the  $VH$  configuration.

ers only  $S$ -scattered waves<sup>12</sup> and thus the calculated result cannot distinguish between forward and backward scattering of the light.

When we compare the  $VV$  with the  $VH$  configurations for the polarized light, the Raman intensity shows anisotropic behavior. Most importantly, the  $A_{1g}$  mode at  $165\text{ cm}^{-1}$  is suppressed in the  $VH$  configuration, while the lower-frequency  $E_{1g}$  and  $E_{2g}$  modes are not suppressed. This anisotropy is due to the degenerate vibrations of the  $E$  modes, whose eigenfunctions are partners that are orthogonal to each other, thus giving rise to large  $VH$  signals. The Raman intensity is normalized in each figure to the maximum intensity of unity. From the figure we see that the relative intensities for the same lower-frequency  $A_{1g}$  mode between the  $VV$  and  $VH$  polarizations are quite different. However, the absolute values for the intensities for the  $VV$  and  $VH$  polarizations are on the same order for all the  $E$  modes.

It is interesting that the higher  $A_{1g}$  mode does not show much suppression between the  $VV$  and  $VH$  geometries, which is closely related to the direction of the vibrations. Even if the phonon mode is an  $A_{1g}$  mode, we can expect a signal in the  $VH$  geometry if the vibration is not parallel to

the polarization. In fact, in Sec. III B 2 we can see a strong dependence of the Raman intensity on the sample orientation for the  $A_{1g}$  mode. As mentioned in Sec. II, the lattice can be split into two sublattices consisting of  $A$  and  $B$  atoms. In the higher-frequency  $A_{1g}$  mode, the  $A$  and  $B$  atoms move in opposite directions (out of phase) in the unit cell, while in the lower-frequency  $A_{1g}$  mode, the  $A$  and  $B$  atoms move in the same way (in phase). When we investigate the vibration of the higher-frequency  $A_{1g}$  mode, the vibration corresponds to the folded vibration of one of the higher  $E_{2g}$  modes of graphite. Thus, in the cylindrical geometry, we may get a result that is not so polarization sensitive. On the other hand, in  $C_{60}$ , since all 60 atoms are equivalent, no carbon atom can move in an out-of-phase direction around the  $C_5$  axes for either of the two  $A_{1g}$  modes, so that both modes show similar polarization behavior to each other.<sup>1</sup>

When we compare the calculated Raman intensities for armchair, zigzag, and chiral nanotubes of similar diameters, we do not see large differences in the lower-frequency Raman modes. This is because the lower-frequency modes have a long wavelength, in-phase motion, so that these modes cannot see the chirality of the nanotube in detail, but rather the modes see a homogeneous elastic cylinder. However, it is interesting to see whether the Raman intensity is sensitive to the nanotube chirality for the higher-frequency Raman modes. An explanation for the chirality dependence in the higher-frequency Raman modes may come from the curvature of the nanotube as follows. In the high-frequency region, all phonon modes consist of the out-of-phase and in-cylindrical-plane modes that result from the folding of the phonon modes with various  $k$  points of 2D graphite.<sup>20</sup> The out-of-phase modes for a  $C=C$  bond consist of  $C=C$  radial (or bond stretching) motion and tangential in-plane (or bond-bending) motion, in which the tangential motion is perpendicular to the radial motion. The Raman-active  $E_{2g}$  mode of 2D graphite at  $1582\text{ cm}^{-1}$  corresponds to  $C=C$  bond-stretching motions for one of the three nearest-neighbor bonds in the unit cell. A similar motion in a nanotube should be expected to give a large Raman intensity. When we see the motion of the Raman-active modes of a nanotube, we can consider an envelope function for the amplitude of the vibration, multiplying it by the above-mentioned out-of-phase motions. We can say that the envelope function should satisfy the selection rules for Raman-active modes among the many phonon modes. For example, the envelope functions for the  $A_{1g}$ ,  $E_{1g}$  and  $E_{2g}$  modes are functions with zero, two, and four nodes around the tube  $z$  axis, respectively. Thus the envelope functions with a given symmetry are similar to one another for nanotubes with any  $(n,m)$  values. However, the directions of the out-of-phase motions of the  $A_{1g}$  modes are different for armchair and zigzag nanotubes. In fact, the  $C=C$  bond-stretching motions can be seen in the horizontally and the vertically vibrating  $C=C$  bonds for armchair and zigzag nanotubes, respectively. Thus the curvature of the nanotube affects the frequency of these modes. A similar discussion can be applied to the  $E$  modes or to a chiral nanotube, in which the direction of the out-of-phase mode is affected by the curvature. The ratio of the bond-stretching displacement to the bond-bending displacement in the out-of-phase motions affects the relative intensity of each mode and the relative intensity depends on the chirality of

the nanotube. Although these higher-frequency modes are difficult to distinguish from one another in the experiment because of their similar frequencies, it should be possible to identify the different modes experimentally, once purified, aligned, single-wall nanotube samples become available, as shown in Sec. III B 2, where the angular dependence of the Raman intensities is discussed.

It could be very interesting to discuss the Raman frequencies in the intermediate frequency region where the frequency may show the greatest chirality dependence.<sup>21</sup> The calculated results, however, show almost no intensity for the intermediate Raman modes around  $1200\text{--}1500\text{ cm}^{-1}$ . The Raman experiments on single-wall nanotubes show weak peaks that have been assigned to armchair modes.<sup>4</sup> From the calculation we cannot explain why these low-intensity peaks appear. The peaks might come from a lowering of the symmetry of the nanotube. In fact, broad Raman peaks around  $1350\text{ cm}^{-1}$  are observed in the experiment.<sup>4,22</sup> Broad peaks around  $1350\text{ cm}^{-1}$  are known to be associated with symmetry-lowering effects in disordered graphite<sup>23</sup> and in carbon fibers.<sup>15</sup> The relative intensity of the broad peak around  $1350\text{ cm}^{-1}$  to the strong  $E_{2g}$  mode at  $1582\text{ cm}^{-1}$  is sensitive to the lowering of the crystal symmetry of graphite,<sup>23,24</sup> and the amount of disorder in carbon fibers<sup>15</sup> and in graphite nanoclusters<sup>25</sup> can be controlled by the heat treatment temperature  $T_{HT}$  or by ion implantation.<sup>26</sup> The non-zone-center phonon mode at  $1365\text{ cm}^{-1}$  has a flat energy dispersion around the  $M$  point in the Brillouin zone of graphite, which implies a high phonon density of states.<sup>27</sup> Moreover, in small aromatic molecules, though the frequency and the normal mode displacements are modified by the finite-size effect, these  $M$ -point phonon modes become Raman active<sup>28</sup> and have a large intensity.<sup>25,29</sup> Thus some symmetry-lowering effects such as the effect of the end caps, the bending of the nanotube, and other possible defects are likely to give rise to Raman intensity for this  $M$ -point mode. Note that if the nanotube is deformed to a  $2\times 2$  structure for any reason, the  $M$  point phonon can be folded to the  $\Gamma$  point and the folded modes become Raman-active  $A_g$  modes. However, since a Peierls instability is unlikely, this situation may occur only in the case of intercalated nanotubes<sup>22</sup> or when there is orientational ordering of the nanotubes in the rope.

As is noted in the Introduction, it is important to consider the resonance effect when discussing Raman intensities. Although the three nanotubes in Fig. 5 have similar radii, the number of carbon atoms per 1D unit cell is very different. For example, the (10,10) and (17,0) nanotubes have 40 and 68 carbon atoms in their 1D unit cells, respectively. However, the (11,8) nanotube has 364 carbon atoms in its unit cell. The singularities in the electronic density of states are difficult to observe in the (11,8) nanotube within the resolution of the scanning tunneling microscope and thus the resonant Raman effect for chiral nanotubes should also be relatively difficult to observe compared to the case of achiral nanotubes. It would be interesting to be able to assign the chirality of a nanotube from the Raman spectra by using many laser excitation frequencies.

## 2. Sample orientation dependence

Finally, we show the Raman intensity of the (10,10) armchair nanotube as a function of sample orientation. Here we

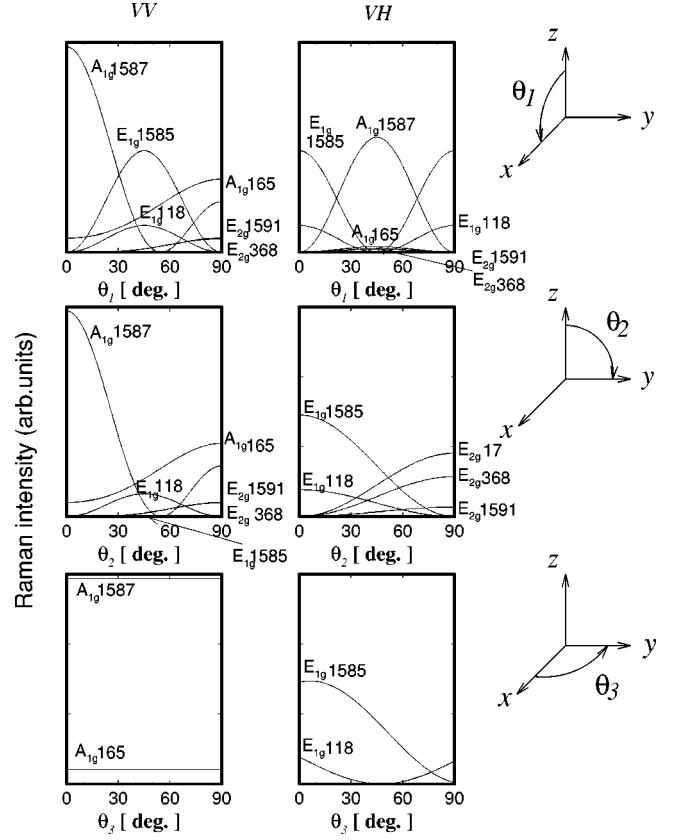


FIG. 6. Raman intensities as a function of the sample orientation for the (10,10) armchair nanotube. As shown on the right,  $\theta_1$  and  $\theta_2$  are angles of the nanotube axis from the  $z$  axis to the  $x$  axis and  $y$  axis, respectively.  $\theta_3$  is the angle of the nanotube axis around the  $z$  axis from the  $x$  axis to the  $y$  axis. The left- and right-hand figures correspond to the  $VV$  and  $VH$  polarizations. The  $E_{2g}$  modes at  $368$  and  $1591\text{ cm}^{-1}$  are almost on the same curve in the figures except for the  $VH$  ( $\theta_2$ ) configuration.

rotate the nanotube axis from the  $z$  axis by fixing the polarization vectors to lie along the  $z$  and  $x$  axes, respectively, for the  $V$  and  $H$  polarizations. In this geometry, three rotations of the nanotube axis are possible for the  $VV$  and the  $VH$  configurations and these three rotations are denoted by  $\theta_i$  ( $i=1,2,3$ ). Here  $\theta_1$  and  $\theta_2$  are the angles of the nanotube axis from the  $z$  axis to the  $x$  and  $y$  axes, respectively, while  $\theta_3$  is the angle of the nanotube axis around the  $z$  axis from the  $x$  to the  $y$  axis. Since we put the horizontal polarization vector along the  $x$  axis,  $\theta_1$  and  $\theta_2$  are different from each other for the  $VH$  configuration. Even for the  $VV$  configuration the rotations by  $\theta_1$  and  $\theta_2$  are not equivalent to each other in the case of the (10,10) armchair since the (10,10) armchair nanotube has a tenfold symmetry axis ( $C_{10}$ ) that is not compatible with the Cartesian axes. Here we define the  $x, y, z$  axes so that we put a carbon atom along the  $x$  axis when  $\theta_3=0^\circ$ . In Fig. 6 we show the relative Raman intensities for the (10,10) armchair nanotube for the  $VV$  and  $VH$  configurations as a function of  $\theta_i$  ( $i=1,2,3$ ).

When we see the Raman intensity as a function of  $\theta_1$ , the  $A_{1g}$  mode at  $1587\text{ cm}^{-1}$  has a maximum at  $\theta_1=0$ , which corresponds to  $\theta_2=\theta_3=0$  for the  $VV$  configuration, while the  $E_{1g}$  mode at  $1585\text{ cm}^{-1}$  has a maximum at  $\theta_1=45^\circ$ . When  $\theta_1$  increases to  $45^\circ$ , the relationship between the in-

intensities of the  $A_{1g}$  mode at  $1587\text{ cm}^{-1}$  and the  $E_{2g}$  mode at  $1585\text{ cm}^{-1}$  becomes reversed for both the  $VV$  and  $VH$  configurations. Thus we can distinguish these two close-lying modes from each other experimentally if we have an axially aligned nanotube sample. There is also an  $E_{2g}$  mode at  $1591\text{ cm}^{-1}$  that can be distinguished from the  $A_{1g}$  and  $E_{1g}$  modes since the  $E_{2g}$  mode has a maximum at  $\theta_1 = 90^\circ$ . As for the other Raman-active modes, we can also distinguish them by their frequencies and polarizations. Even the modes belonging to the same irreducible representation do not always have the same basis functions since we have two inequivalent atoms  $A$  and  $B$  in the hexagonal lattice. For example, the  $A_{1g}$  mode at  $165\text{ cm}^{-1}$  has a different functional form from the  $A_{1g}$  mode at  $1587\text{ cm}^{-1}$ .

From Fig. 6 it is seen that the angular dependences of almost all the Raman intensities on  $\theta_1$  and  $\theta_2$  are similar to each other for the  $VV$  configuration, except for the  $E_{1g}$  mode at  $1585\text{ cm}^{-1}$ . The difference of the  $E_{1g}$  modes between  $\theta_1$  and  $\theta_2$  at  $1585\text{ cm}^{-1}$  is due to the form of the basis function. There is also a symmetry reason why we can see only  $A$  modes and  $E$  modes in the  $VV$  ( $\theta_3$ ) and the  $VH$  ( $\theta_2$  and  $\theta_3$ ) configurations, respectively. On the other hand, we can see that there are some very weak intensities in the figure since the triangular lattice of the nanotube ropes is incompatible with the tenfold symmetry axis. Even if we get an aligned sample in the  $z$  axis, the  $xy$  direction of the constituent nanotubes should be random since the tenfold symmetry of the (10,10) nanotube does not satisfy the symmetry of the triangular nanotube lattice. Thus an averaged angular dependence for  $\theta_1$  and  $\theta_2$  is expected for a general aligned sample. Even in this case, since the  $A_{1g}$  modes at  $165\text{ cm}^{-1}$  and  $1587\text{ cm}^{-1}$  are independent of  $\theta_3$ , this signal will be clearly seen. It is pointed out that the (9,9) armchair nanotube is thus of special interest since it is one of a few examples where the

$n$ -fold symmetry of the nanotube can match the lattice symmetry operations, for which detailed angular-dependent selection rules can be expected.

#### IV. SUMMARY

In summary, we have investigated the Raman intensity of armchair, zigzag, and chiral nanotubes as a function of their polarization geometry and sample orientation. We found that there is no significant dependence on chiral angle of the intensity for the lower-frequency Raman modes below  $500\text{ cm}^{-1}$  for carbon nanotubes, while the higher-frequency Raman modes have different relative intensities depending on their chiralities. The resonant Raman intensity may depend on the number of carbon atoms in the unit cell. The sample orientation dependence of the Raman intensity shows that not only the symmetry but also the direction of the displacements gives rise to its own angular dependence, which can be used for distinguishing between the symmetry assignments for the higher-frequency Raman modes. Such a symmetry analysis will also be useful for identifying the chirality of carbon nanotubes.

#### ACKNOWLEDGMENTS

The authors thank Nakadaira Masao, Manyalibo Matthews, Dr. H. Kataura, and Dr. E. Richter for stimulating discussions. R.S., G.D., and M.S.D. thank the International Joint Research Program of the New Energy and Industrial Technology Organization (NEDO), Japan for its support. Part of the work by R.S. was supported by a Grant-in-Aid for Scientific Research (Grants Nos. 08454079 and 9243211) from the Ministry of Education and Science of Japan. The MIT work was partly supported by the NSF (Grant No. DMR 95-10093).

- 
- <sup>1</sup>M. S. Dresselhaus, G. Dresselhaus, and P. C. Eklund, *Science of Fullerenes and Carbon Nanotubes* (Academic, New York, 1996).
- <sup>2</sup>T. Guo, C.-M. Jin, and R. E. Smalley, *Chem. Phys. Lett.* **243**, 49 (1995).
- <sup>3</sup>A. Thess, R. Lee, P. Nikolaev, H. Dai, P. Petit, J. Robert, C. Xu, Y. H. Lee, S. G. Kim, A. G. Rinzler, D. T. Colbert, G. E. Scuseria, D. Tománek, J. E. Fischer, and R. E. Smalley, *Science* **273**, 483 (1996).
- <sup>4</sup>A. M. Rao, E. Richter, S. Bandow, B. Chase, P. C. Eklund, K. W. Williams, M. Menon, K. R. Subbaswamy, A. Thess, R. E. Smalley, G. Dresselhaus, and M. S. Dresselhaus, *Science* **275**, 187 (1997).
- <sup>5</sup>R. Saito, M. Fujita, G. Dresselhaus, and M. S. Dresselhaus, *Phys. Rev. B* **46**, 1804 (1992).
- <sup>6</sup>M. S. Dresselhaus, G. Dresselhaus, and R. Saito, *Carbon* **33**, 883 (1995).
- <sup>7</sup>H. Kataura *et al.* (unpublished).
- <sup>8</sup>J. Yu, K. Kalia, and P. Vashishta, *Europhys. Lett.* **32**, 43 (1995).
- <sup>9</sup>J. M. Cowley, P. Nikolaev, A. Thess, and R. E. Smalley, *Chem. Phys. Lett.* **265**, 379 (1997).
- <sup>10</sup>R. A. Jishi, L. Venkataraman, M. S. Dresselhaus, and G. Dresselhaus, *Chem. Phys. Lett.* **209**, 77 (1993).
- <sup>11</sup>O. Madelung, *Solid State Theory* (Springer-Verlag, Berlin, 1978).
- <sup>12</sup>S. Guha, J. Menéndez, J. B. Page, and G. B. Adams, *Phys. Rev. B* **53**, 13 106 (1996).
- <sup>13</sup>D. W. Snoke and M. Cardona, *Solid State Commun.* **87**, 121 (1993).
- <sup>14</sup>B. T. Kelly, *Physics of Graphite* (Applied Science, Englewood, NJ, 1981).
- <sup>15</sup>M. S. Dresselhaus, G. Dresselhaus, K. Sugihara, I. L. Spain, and H. A. Goldberg, in *Graphite Fibers and Filaments* edited by Editor(s), Springer Series in Materials Science Vol. 5 (Springer-Verlag, Berlin, 1988).
- <sup>16</sup>M. M. J. Treacy, T. W. Ebbesen, and J. M. Gibson, *Nature (London)* **381**, 678 (1996).
- <sup>17</sup>B. I. Yakobson and R. E. Smalley, *Am. Sci.* **85**, 324 (1997).
- <sup>18</sup>D. H. Robertson, D. W. Brenner, and J. W. Mintmire, *Phys. Rev. B* **45**, 12 592 (1992).
- <sup>19</sup>J. W. Mintmire and C. T. White, *Carbon* **33**, 893 (1995).
- <sup>20</sup>A. Kasuya, Y. Sasaki, Y. Saito, K. Tohji, and Y. Nishina, *Phys. Rev. Lett.* **78**, 4434 (1997).
- <sup>21</sup>P. C. Eklund, J. M. Holden, and R. A. Jishi, *Carbon* **33**, 959 (1995).
- <sup>22</sup>A. M. Rao, P. C. Eklund, S. Bandow, A. Thess, and R. E. Smalley, *Nature (London)* **388**, 257 (1997).

- <sup>23</sup>F. Tuinstra and J. L. Koenig, *J. Chem. Phys.* **53**, 1126 (1970).
- <sup>24</sup>P. Lespade, R. Al-Jishi, and M. S. Dresselhaus, *Carbon* **20**, 427 (1982).
- <sup>25</sup>M. J. Matthews, X. X. Bi, M. S. Dresselhaus, M. Endo, and T. Takahashi, *Appl. Phys. Lett.* **68**, 1078 (1996).
- <sup>26</sup>M. S. Dresselhaus and R. Kalish, in *Ion Implantation in Diamond, Graphite and Related Materials*, edited by U. Sonser *et al.* Springer Series in Materials Science Vol. 22 (Springer-Verlag, Berlin, 1992).
- <sup>27</sup>R. Al-Jishi and G. Dresselhaus, *Phys. Rev. B* **26**, 4514 (1982).
- <sup>28</sup>K. Yoshizawa, K. Okahara, T. Sato, K. Tanaka, and T. Yamabe, *Carbon* **32**, 1517 (1994).
- <sup>29</sup>S. Krichene, J. P. Buisson, and S. Lefrant, *Synth. Met.* **17**, 589 (1986).